Cryo-EM structure of pro-aggregant P301L/S320F double-mutant tau filaments formed in mouse brains following peripheral AAV delivery

Authors

Maria Kano[1#], Taeko Kimura[1#], Haruaki Yanagisawa[2#], Lisa Tatsumi[1], Komei Yamashita[1], Asahi Sakai[1], Xinyi Li[1], Takaomi C. Saido[3], Takashi Saito[4], Sho Takatori[1], Masahide Kikkawa[2], Taisuke Tomita[1*]

Author Information

[1]Laboratory of Neuropathology and Neuroscience, Graduate School of Pharmaceutical Sciences, The University of Tokyo, 7-3-1 Hongo, Bunkyo-ku, Tokyo 113-0033, Japan

[2]Department of Cell Biology and Anatomy, Graduate School of Medicine, The University of Tokyo, 7-3-1 Hongo, Bunkyo-ku, Tokyo 113-0033, Japan

[3]Laboratory for Proteolytic Neuroscience, RIKEN Center for Brain Science, 2-1 Hirosawa, Wako, Saitama 351-0198, Japan

[4]Department of Neurocognitive Science, Institute of Brain Science, Nagoya City University Graduate School of Medical Science, 1 Kawasumi, Mizuho-cho, Mizuho-ku, Nagoya, Aichi 467-8601, Japan

[#]These authors contributed equally to this work.

*Corresponding author

Correspondence, Taisuke Tomita, The University of Tokyo, Tokyo, Japan.

Email: taisuke@mol.f.u-tokyo.ac.jp

Abstract

Tauopathies are characterized by the accumulation of abnormally phosphorylated tau filaments, with disease-specific folds revealed by cryo-electron microscopy (cryo-EM). Here, we delivered a recombinant human tau carrying the P301L/S320F double mutation into *App*$^{NL\text{-}G\text{-}F}$/*MAPT* double knock-in mice using a blood-brain-barrier-permeable AAV (AAV-PHP.eB), enabling rapid induction of tau aggregation *in vivo*. The mutant tau was systemically administered via retro-orbital injection, providing a minimally invasive approach for widespread neuronal transduction. Phosphorylated tau aggregation, as well as seeding activity, were observed without the need for exogenous seeds. Our cryo-EM analysis resolved a novel filament fold incorporating residues 279-329, in which the P301L and S320F mutations introduced stabilizing interactions that reinforced filament assembly. This conformation was distinct from previously reported folds, including Alzheimer and Pick tau filaments. Moreover, the filaments adopted a more compact architecture than those observed in patient-derived samples or other model mice. This finding demonstrates that P301L/S320F double-mutant tau adopts a structurally unique, highly aggregation-prone fold, and that this system provides a rapid platform for modeling tau filament formation.

Keywords

Alzheimer disease, cryo-EM, Pick disease tau, tauopathy

Introduction

Tauopathies comprise a spectrum of neurodegenerative disorders defined by intracellular inclusions of abnormally phosphorylated and aggregated microtubule-associated protein tau, which is encoded by the Microtubule-Associated Protein Tau *(MAPT*) gene. These disorders include Alzheimer disease (AD), frontotemporal dementia (FTD), Pick's disease (PiD), and corticobasal degeneration. In these conditions, the accumulation of tau filaments, known as neurofibrillary tangles (NFTs), is closely associated with progressive neurodegeneration and synaptic dysfunction [1,2].

Tau is an intrinsically disordered protein that stabilizes and dynamically regulates microtubules. The human *MAPT* gene generates six isoforms through alternative splicing, which differ in the number of microtubule-binding repeats (three-repeat (3R) or four-repeat (4R)) and the presence or absence of N-terminal inserts (Supplementary Fig. 1) [1]. In the adult human brain, 3R and 4R tau isoforms are expressed at approximately equal ratios, whereas murine brains predominantly express 4R tau [3]. The binding of tau to microtubules is tightly regulated by its phosphorylation state [4], and dysregulation of this balance is thought to underlie the onset of pathological aggregation. Notably, the discovery of pathogenic MAPT mutations in families with FTDP-17 provided strong genetic evidence that tau dysfunction is sufficient to cause neurodegeneration, and linked tau aggregation pathology to the pathogenesis of tauopathies [5,6].

In AD brains, aggregated tau forms paired helical filaments (PHFs) [7], which assemble into NFTs. This filament structure exhibits an AD-specific fold that reflects the disease's molecular identity [8–10]. These filaments propagate in a prion-like manner

70 between neurons, driving the stepwise regional spread of NFTs described by Braak
71 staging [11]. The progression of NFT pathology correlates strongly with neuronal loss
72 and cognitive decline [11,12], suggesting that tau filament accumulation directly drives
73 neurodegeneration. Filamentous tau is not only hyperphosphorylated but also modified
74 by ubiquitination [13–15], acetylation [16,17], and SUMOylation [18], among other post-
75 translational modifications.

76 The advent of cryo-electron microscopy (cryo-EM) technology has enabled near-
77 atomic structural determination of tau filaments isolated from tauopathy patient brains
78 [8–10]. These structural studies have substantially advanced our understanding of the
79 molecular mechanisms underlying tau aggregation and the pathological heterogeneity of
80 tau-related disorders.

81 In parallel, *in vivo* modeling of tau pathology has advanced considerably.
82 Transgenic mice expressing tauopathy-associated mutations [19] and models involving
83 intracerebral inoculation of patient-derived [20] or recombinant tau filaments [21,22]
84 have provided invaluable insights into the mechanisms of tau propagation and filament
85 formation. More recently, expression of the P301L/S320F double-mutant tau—
86 combining the frontotemporal dementia and Parkinsonism linked to chromosome 17
87 (FTDP-17)–associated P301L mutation [23,24] and the PiD-associated S320F mutation
88 [25,26]—via adeno-associated virus (AAV) injection into neonatal mouse ventricles has
89 been shown to induce robust tau aggregation within a short period [27]. This approach
90 has attracted attention as a rapid and reproducible model of tau filament formation.

91 In this study, we sought to develop a less invasive and efficient *in vivo* model of

92 AD-related tau pathology and to elucidate the structural determinants underlying the
93 marked aggregation propensity of tau by analyzing the filamentous structures formed in
94 this model. To this end, we utilized the AAV-PHP.eB system, a modified AAV9 variant
95 that enables highly efficient central nervous system transduction following systemic
96 administration, and expressed P301L/S320F mutant human tau *via* retro-orbital venous
97 injection [28,29]. The AAV-PHP.eB serotype is reported to cross the blood–brain barrier
98 following systemic administration efficiently and to robustly transduce cortical and
99 hippocampal neurons, offering a less invasive alternative to direct intracranial injection.
100 For the recipient mouse, we used humanized tau knock-in mice with an amyloid plaque–
101 forming background ($App^{NL\text{-}G\text{-}F}$/*MAPT* double knock-in mice), in which the murine *App*
102 and *Mapt* genes are replaced by the human *APP* exons carrying familial AD-linked
103 mutations as well as the *MAPT* locus, respectively [30]. This mouse model expresses both
104 3R and 4R human tau isoforms under endogenous control [31], with a comparable balance
105 of tau isoforms to that observed in the human brain and also accumulates amyloid-β (Aβ)
106 [30], thereby allowing investigation of tau aggregation within a genetic and pathological
107 milieu that closely resembles the human AD brain.

108 Following systemic administration of AAV-PHP.eB encoding P301L/S320F
109 mutant human tau, phosphorylated tau–positive aggregates were induced within
110 approximately 1.5 months in a minimally invasive manner. Biochemical and cryo-EM
111 analyses of sarkosyl-insoluble fractions revealed tau filaments with a near-atomic fold.
112 These findings provide mechanistic insight into how the P301L/S320F mutation enhances
113 tau aggregation propensity and support the emergence of a unique filament structure
114 formed in a human tau background.

115 **Material and methods**

116 **Mouse and cell culture**

117 *App*$^{NL\text{-}G\text{-}F}$/*hMAPT* double knock-in mice were maintained on a C57BL/6J
118 background [32]. HEK293A cell was a kind gift from Dr. Hidenori Ichijo (The University
119 of Tokyo)[33,34]. Biosensor (BS) cells, which provide a fluorescence resonance energy
120 transfer (FRET) signal by seeding-competent tau filaments, were purchased from ATCC
121 (CRL-3275). The cells were cultured as previously described [35,36].

122

123 **Extraction of the tau filaments from culture cells**

124 Cells were resuspended in 1 mL of phosphate-buffered saline (PBS) and
125 centrifuged at 4,500 × g for 5 min at 25 °C. The resulting pellets were resuspended in 300
126 μL of lysis buffer containing 1% sarkosyl in A68 buffer (10 mM Tris–HCl, pH 7.5, 10%
127 sucrose, 0.8 M NaCl, and 1 mM EGTA) [37], followed by sonication using HG-30
128 homogenizer (Hitachi). An additional 300 μL of lysis buffer was then added, and the
129 samples were centrifuged at 168,000 × g (S55A2-2698 roter, Himac) for 20 min at room
130 temperature. The supernatant (soluble fraction) and pellet (insoluble fraction) were
131 collected separately [38,39]. Protein concentrations in the supernatant were determined
132 using a BCA assay, and 5× SDS sample buffer was added. The pellet fractions were
133 resuspended in 50 μL of 2 × SDS sample buffer for western blotting, followed by brief
134 sonication. All samples were heated at 100 °C for 5 min prior to electrophoresis. Prepared
135 samples were separated by SDS–PAGE and transferred onto polyvinylidene difluoride
136 (PVDF) membranes (Millipore) as described[35]. The list of primary antibodies and their

137 dilution ratios is provided in Tables S1 and S2.

138

139 **Fluorescence resonance energy transfer (FRET)**

140 BS cells were seeded into 24-well plates, and 20 μg of mouse brain homogenate
141 was added to each well. The homogenate was mixed with Lipofectamine 2000 (Thermo
142 Fisher Scientific) at 1.47 μL per well, incubated for 15 min at room temperature, and then
143 applied to the cells. After treatment, the cells were cultured for 72 h. After incubation,
144 cells were washed with PBS, detached by trypsinization, and resuspended in PBS
145 containing 20% FBS. FRET signals were measured by flow cytometry using the MA900
146 cell sorter (SONY), with the increase in acceptor fluorescence upon donor excitation as
147 the readout. The percentage of FRET-positive cells was calculated as described [40].

148

149 **Electron microscopy**

150 For electron microscopy of cultured cell-derived tau filaments, pellet fractions
151 were resuspended in 50 μL of Tris buffer (10 mM Tris-HCl, pH 7.4, 1 mM DTT, 1 mM
152 EGTA). After sarkosyl fractionation of brain homogenates, the sarkosyl-insoluble pellet
153 was resuspended in 10 μL of physiological saline, and 1.5 μL was applied onto collodion-
154 coated 200 mesh copper grids (Nisshin EM Co). Negative staining was performed with
155 2% phosphotungstic acid. Samples were examined using a transmission electron
156 microscope (JEM-1200EXII, JEOL) operated at an acceleration voltage of 80 kV. Images
157 were acquired at magnifications ranging from 12,000× to 200,000× using a CCD camera
158 (Veleta, JEOL) controlled with iTEM software (Olympus Soft Imaging Solutions). For

159 immuno-electron microscopy, purified tau filaments were adsorbed onto collodion-coated
160 200 mesh copper grids (Nisshin EM Co.) for 30 s, followed by blocking with PBS
161 containing 1% gelatin for 10 min and incubation with primary antibodies for 1 h. The
162 grids were then washed with blocking buffer and incubated with 10 nm gold-conjugated
163 anti-rabbit IgG or 5 nm gold-conjugated anti-mouse IgG (1:50 in blocking buffer) for 1 h
164 (Table S1, 2). After washing with water, the samples were negatively stained with 2%
165 PTA for 90 s[41].

166

167 **Recombinant AAV system**

168 A recombinant AAV system of the PHP.eB [42] serotype was used to express
169 human 1N4R MAPT carrying the P301L and S320F mutations. The expression cassette
170 consists of the human MAPT cDNA with the P301L/S320F mutation under the control of
171 the human synapsin I promoter, followed by a woodchuck hepatitis virus post-
172 transcriptional regulatory element (WPRE) and a polyadenylation signal. The expression
173 cassette was inserted into the pAAV-hSyn1-eYFP backbone (Addgene plasmid #117382)
174 [29]. The eYFP coding sequence was removed by digestion with EcoRI and KpnI, and
175 the MAPT insert was introduced using HiFi DNA Assembly (New England Biolabs). The
176 recombinant AAV viruses used for mouse injections were produced and purified by the
177 Department of Neurodegenerative Medicine, Gunma University Graduate School of
178 Medicine. Recombinant virus production was carried out in HEK293T cells using the
179 triple plasmids; pAAV-hSyn1-tau-WPRE, pHelper (Agilent Technologies), pAAV-
180 PHP.eB [43,44]. AAV-PHP.eB were produced using the ultracentrifugation method
181 described in a previous paper[43]. For *in vivo* experiments, recombinant viruses were

182 delivered to mice via the retro-orbital sinus at a titer of 2–5 × 10^{11} vg per mouse.

183

184 **Immunohistochemistry and image quantification**

185 Immunohistochemical analyses were performed as previously described [45].
186 Stained sections were examined using fluorescence microscopy (BZ-X800, Keyence).
187 High-resolution tiled images of AT8, AT180, PHF-1, and pS396 were reconstructed by
188 stitching without compression, and exported using the Keyence analyzer package (BZ-X
189 series). For the quantitative analysis of protein associations with phospho-tau lesions, we
190 used a 20 × objective lens. Regions of interest were manually selected and cropped from
191 the acquired images based on anatomical landmarks. The percentage of areas stained by
192 AT8, AT180, PHF-1, and pS396 in selected brain regions was quantified using the BZ-
193 X800 Analyzer Hybrid Cell Count Module (Keyence). Parameters were set to a threshold
194 of control and applied automatically to all images within the proper comparisons. To
195 minimize the influence of background staining and potential artifacts, AT8- or pS396-
196 positive regions exceeding 10,000 μm^2 in area were excluded from the quantification.
197 This threshold was set to filter out abnormally large signals likely due to non-specific
198 staining. Statistical analyses were conducted using R software (version 4.5.1). Group
199 means were compared using one-way analysis of variance (ANOVA), followed by
200 Tukey's Honest Significant Difference (HSD) test for post-hoc analysis ($*p < 0.05$).

201

202 **Sampling of mouse brains for western blotting**

203 Fractionation of mouse brains for western blotting was performed as previously

204 described with some modifications [46]. Half brains were homogenized in 10 volumes of
205 homogenization buffer (10 mM Tris-HCl, pH 7.4, 1 mM EGTA, 1 mM EDTA, 0.8 M
206 NaCl, 10% sucrose, supplemented with PhosSTOP (Sigma) and a protease inhibitor
207 cocktail (cOmplete™ ULTRA, 1 tablet/50 mL; Roche) using a HG-30 homogenizer. The
208 homogenates were ultracentrifuged at 168,000 × g for 20 min at 25 °C with an S55A2-
209 2698 rotor. Sarkosyl was then added to the supernatant at a final concentration of 2%,
210 followed by shaking at 37 °C for 30 min. After sonication, the samples were centrifuged
211 at 20,000 × g for 20 min at 25 °C with an S55A2-2698 rotor, and the resulting supernatant
212 was further ultracentrifuged at 168,000 × g for 20 min at 25 °C using an S55A2-2698
213 rotor. The pellet was resuspended in homogenization buffer containing 1% sarkosyl and
214 subjected to the same centrifugation cycle. The final pellet was resuspended in Tris buffer,
215 mixed with an equal volume of 2× SDS sample buffer, and boiled at 100 °C for 10 min
216 to obtain the sarkosyl-insoluble fraction. Supernatants obtained at each centrifugation
217 step were combined with sample buffer and used as sarkosyl-soluble fractions.

218

219 **Extraction of the tau filaments from mouse brains**

220 Mouse brains were weighed and homogenized in 10 volumes (w/v) of
221 homogenization buffer. Homogenization was performed using the HG-30 homogenizer
222 (Hitachi). The homogenates were centrifuged at 11,400 × g (SW41Ti rotor, Beckman
223 Coulter) for 10 min at room temperature, and the supernatants were collected. The
224 supernatants were then centrifuged at 183,000 × g (SW41Ti rotor) for 4 h at 25 °C. The
225 resulting pellets were resuspended in 1% sarkosyl solution prepared with half the volume
226 of the original tissue buffer and incubated at 37 °C for 60 min with shaking. After

227 incubation, the suspensions were centrifuged at 12,100 × g for 20 min at 25 °C (S55A2-
228 2698 rotor), and the supernatants were collected. These supernatants were further
229 centrifuged at 168,000 × g for 20 min at 25 °C (S55A2-2698 rotor), and the resulting
230 pellets were resuspended in 10 mL of tissue buffer. To remove contaminating components,
231 the suspension was treated with 0.2 mg/mL collagenase (Sigma-Aldrich), 2 mM $MgCl_2$,
232 0.5 mM $CaCl_2$, and 200 U/mL DNase I (Takara), followed by shaking at 200 rpm at 37 °C
233 for 1 h. After enzymatic digestion, the final concentration of NaCl was adjusted to 1 M,
234 and Triton X-100 was added to 0.5% (v/v). The mixture was further incubated at 37 °C
235 for 30 min with shaking. To precipitate proteins, three volumes of pre-chilled methanol
236 at –30 °C were added, and the samples were incubated for 30 min at –30 °C, followed by
237 centrifugation at 20,000 × g for 30 min at 4 °C. The resulting pellets were resuspended in
238 10 mL of 5% sarkosyl solution. Subsequently, the following fractionation steps were
239 repeated: centrifugation at 11,400 × g for 20 min at 25 °C to remove debris, followed by
240 centrifugation of the supernatants at 168,000 × g for 30 min at 25 °C (S55A2-2698 rotor).
241 The resulting pellets were resuspended in 2 mL of 5% sarkosyl solution, homogenized by
242 passing through a 25-gauge needle (Terumo), and sequentially treated with 2% and 1%
243 sarkosyl solutions in the same manner. At each step, the suspensions were mixed
244 thoroughly by pipetting (100 times) before centrifugation. Finally, the pellets obtained
245 were resuspended in 500 μL of 1% sarkosyl solution, homogenized again by pipetting,
246 and centrifuged at 168,000 × g for 30 min (S55A2-2698 rotor). The final pellets,
247 containing the sarkosyl-insoluble tau filaments, were collected and stored at –80 °C until
248 use.

249

250 **Cryo-Electron Microscopy (cryo-EM)**

251 Samples were resuspended in cryo-EM buffer (50 mM Tris-HCl (pH 7.4), 1 mM
252 DTT, 0.04% sarkosyl [47]). A 2 µl aliquot of the sample was applied to each side of
253 freshly glow-discharged UltrAuFoil R1.2/1.3 300 mesh grids (Quantifoil Micro Tools
254 GmbH). The grids were blotted from both sides for 4 seconds at 12°C under 100%
255 humidity and subsequently plunge-frozen in liquid ethane using a Vitrobot Mark IV
256 (Thermo Fisher Scientific).

257 Images were recorded on a CRYO ARM 300 II (JEOL, Tokyo, Japan), operated
258 at 300 kV, equipped with an Omega filter whose slit width was set to 20 eV, and a Gatan
259 K3 direct electron detector in correlated-double sampling (CDS) mode. The nominal
260 magnification was set to 60,000×, yielding a physical pixel size of 0.878 Å/pixel. Movies
261 were acquired using the SerialEM software [48], with a target defocus range of -0.8~-1.8
262 µm. Each movie was recorded with a total electron dose of 50 e^{-}/ $Å^2$, divided into 50
263 frames.

264

265 **Data processing of Cyro-EM data**

266 Raw movie frames were motion-corrected, and the contrast transfer function
267 (CTF) was estimated using the Patch CTF function on cryoSPARC v4.7.1[49]. Fibrils
268 were automatically picked using the filament tracer tool, and segments were extracted
269 with a box size of 420 pixels scaled to 300 pixels and an inter-box distance set to 10% of
270 the box size. Several rounds of 2D classification were performed to exclude bad classes
271 that lacked discernible helical twists and non-amyloid contaminants. Initial helical

parameters were estimated from 2D class averages with a box size of 1000 pixels scaled to 750 pixels, and an initial reference was generated using the relion_helix_inimodel2d program [50]. The helical refinement was performed using local helical parameter searches in cryoSPARC. After further local and global CTF refinement, reference-based motion correction, and 3D classification, the particle coordinates were converted into Relion STAR format using UCSF pyem [51] with in-house modifications to convert metadata generated by the filament tracer tool to Relion's counterparts. Relion v5.0 [52,53] was used for further CTF refinement and the 3D auto-refine with local helical parameter searches.

Model building and refinement

An initial model was generated using ModelAngelo[53], and the model was refined using Coot v0.9.8.1 [54], Phenix v1.21.2-5419 [55], and Servalcat v0.4.105 [56]. The refined models were validated using Phenix. Image rendering was performed using UCSF ChimeraX [57] and MaskChains tool [58]. The schematic figures were produced using atom2svg.py [59].

289 **Result**

290 **P301L/S320F double-mutant tau induced tau aggregation in cultured cells.**

291 In the human brain, six tau isoforms are generated by combinations of the
292 number of microtubule-binding repeats,3R or 4R, and the presence of 0, 1, or 2 N-
293 terminal insertions (Fig. S1).To partially recapitulate this isoform expression of the 3R
294 and 4R pattern, we generated HEK293A-derived cell lines that stably express the
295 representative 3R and 4R tau isoforms, 1N3R and 1N4R human tau. We then transfected
296 these cells with a plasmid encoding the 1N4R P301L/S320F mutant tau (Fig. 1a). Three
297 days after transfection, cells were collected and separated into sarkosyl-soluble and -
298 insoluble fractions (Fig. 1b). Western blot analysis showed that P301L/S320F double-
299 mutant tau was prominently detected in the sarkosyl-insoluble fraction, exhibiting a
300 higher signal compared with wild-type (WT) tau. This finding indicates that the
301 P301L/S320F mutation promoted the tau aggregation in cells, as previously described
302 (Fig. 1c, d). Furthermore, electron microscopy of the sarkosyl-insoluble fraction revealed
303 fibrillar structures with a twisted morphology and a diameter of approximately 20 nm
304 (Fig. 1e). Taken together, these findings suggest that P301L/S320F tau can promote
305 highly intracellular aggregation and filament formation.

306

307 **AAV-PHP.eB–mediated delivery of P301L/S320F double mutant tau induces intracellular tau**
308 **aggregation in the mouse brain.**

309 In AD, tau aggregation is known to occur subsequent to the accumulation of Aβ.
310 To model this coexisting Aβ and tau pathology *in vivo*, we employed $App^{NL\text{-}G\text{-}F}$/*hMAPT*

311 double knock-in mice [30,32]. This mouse line carries a knock-in human *APP* allele
312 harboring the Swedish (KM670/671NL), Iberian (I716F), and Arctic (E693G) mutations
313 (*App*$^{NL-G-F}$), combined with a knock-in human *MAPT* (a.k.a., *hMAPT*) allele in which the
314 endogenous mouse *Mapt* locus is replaced. In *App*$^{NL-G-F}$ mice, age-dependent deposition
315 of human Aβ begins around 2 months of age and reaches saturation by approximately 8
316 months. To induce tau aggregation under an Aβ-rich background, 9–11-month-old *App*$^{NL-}$
317 $^{G-F}$/*hMAPT* mice were intravenously injected via the retro-orbital sinus with a
318 recombinant AAV-PHP.eB expressing human P301L/S320F double-mutant tau under the
319 human synapsin I promoter. Control groups included mice injected with WT human tau
320 and non-injected mice (Fig. 2a). After two months, the brains were collected, hemisected,
321 and used for immunohistochemical and biochemical analyses (Fig. 2a). AT8
322 immunoreactivity, a marker of pathological tau phosphorylation [60], revealed prominent
323 AT8-positive signals in the CA2 region of the hippocampus and in layer II of the cerebral
324 cortex in mice expressing P301L/S320F double-mutant tau (Fig. 2b). Quantification
325 confirmed significant AT8 accumulation in the medial parietal association area (MPtA)
326 (Fig. 2c, d) and hippocampal CA2 (Fig. 2e, f). Additionally, other antibodies detecting
327 the phosphorylation-dependent tau pathology, such as AT180 [61], anti-pS396 [62], and
328 PHF-1 [60], likewise detected exclusively in mice expressing P301L/S320F tau (Fig. S2–
329 4). Collectively, these findings indicate that P301L/S320F tau robustly induces the
330 formation of phosphorylated tau aggregates *in vivo* without exogenous seeding.

331

332 **Overexpressed P301L/S320F double-mutant tau in the mouse brain acts as a seed with strong**
333 **aggregation propensity.**

334 We then biochemically analyzed the right hemisphere of the brains from *App*$^{NL-}$
335 $^{G-F}$/*hMAPT* mice injected with AAV expressing P301L/S320F tau by sequential sarkosyl
336 fractionation and western blotting (Fig. 3b). Quantification of the amount of the
337 aggregated tau in the sarkosyl-insoluble fraction relative to the soluble fraction was
338 markedly increased in mice expressing P301L/S320F double-mutant tau compared with
339 those expressing WT tau (Fig. 3c). Notably, endogenous 3R as well as 4R tau were also
340 detected within the insoluble fraction. Furthermore, murine endogenous tau was also
341 detected in the sarkosyl-insoluble tau fraction in mice expressing P301L/S320F double-
342 mutant tau (Fig. S5a.b). Pellets from the sarkosyl-insoluble fractions were analyzed by
343 negative-stain electron microscopy using phosphotungstic acid and by immuno-electron
344 microscopy (Fig. 3d). Only in the P301L/S320F group, fibrillar structures were observed
345 that were immunoreactive for TauC4 [8], AT8, and anti-pS396 antibodies (Fig. 3e-g).
346 Finally, we assessed the seeding activity of brain lysates using BS cells [40]. After
347 transfection of the mouse brain homogenates, the proportion of FRET-positive cells was
348 measured by flow cytometry only in the P301L/S320F group. In contrast, WT tau and
349 uninjected controls showed no detectable FRET signal (Fig. S6). These data suggested
350 that the double-mutant tau acted as a seed for endogenous tau protein regardless of repeat
351 numbers or species.

352

353 **Structural analysis of tau filaments derived from mice expressing P301L/S320F mutant tau by**
354 **cryo-EM**

355 To characterize the ultrastructure of tau assemblies formed *in vivo*, we analyzed
356 the sarkosyl-insoluble tau filaments isolated from the mouse brain expressing the
357 P301L/S320F double-mutant tau (PDB: 22JY) by cryo-EM (Fig. S7). The predominant
358 filaments consisted of a single helical filament type (Fig. 4a, b), and the final
359 reconstructed map reached a resolution of 2.24 Å. The filaments exhibited an approximate
360 diameter of 7 nm and a helical pitch of ~35 nm (Fig. 4a, b). The ordered core comprised
361 residues 279–329 of tau, forming five β-strands connected by loops and turns (Fig. 4c, d).
362 These β-strands corresponded to β1 (N279–S285), β2 (H299–L301), β3 (S305–Y310),
363 β4 (V319–C322), and β5 (L325–H329). The five β-strands were stacked to form a layered
364 β-sheet architecture that contributed to filament stabilization. The β-strands were linked
365 by flexible loops, giving the overall structure a gently curved, folded conformation (Fig.
366 4c, d).

367 In addition, three prominent extra densities protruding from the filament surface
368 were observed near lysine residues; although consistently positioned, their molecular
369 identities remain unclear (Fig. 5a, b). The pathogenic residues P301L and S320F were
370 each located within the second and fourth β-strands of the core, respectively. P301L
371 formed hydrophobic interactions with I328 (Fig. 5c), whereas S320F was buried within a
372 loop region, where its aromatic ring engaged in Z-axis π–π stacking that further stabilized
373 the filament. S320F additionally established hydrophobic contacts with Q307, V309,
374 P312, L315, and V318, likely increasing the stability of the entire loop structure (Fig. 5d).

375 These hydrophobic interactions are not present in WT tau, where P301 and S320

are normally solvent-exposed. Therefore, the incorporation of these residues into the filament core represents a structural feature unique to the mutant filaments.

The structure of P301L/S320F mutant tau filaments was distinct from previously reported patient-derived tau filament structures.

To compare the structure of the P301L/S320F mutant tau filaments obtained in this study (magenta) with the structure of tau filaments derived from an FTDP-17 patient carrying the P301L mutation (PDB 9GG0; cyan) [63], we performed structural alignment. The results showed limited similarity, with an RMSD of 4.23 Å over 40 aligned residues (Fig. 6a). In the patient-derived fold, the filament bends at the P301L position, whereas in the P301L/S320F mutant, the filament bends at a different region. Moreover, in our structure, a hydrophobic interaction between P301L and I328—absent in the patient P301L fold—is observed. This is likely due to the S320F-induced folding of a unique loop through extensive hydrophobic interactions, bringing P301L into proximity with I328. The combined effects of P301L- and S320F-mediated interactions appear to rigidify the L301–H329 region, enabling the formation of a second compact loop in which V306 and I308 interlock with L282, L284, and V287 (Fig. 5a, b).

In patients with FTDP-17 carrying the S320F mutation [25,26], Pick bodies composed of 3R tau are observed as a characteristic pathology [64]. We therefore compared our structure with the tau filament derived from PiD (PDB 6GX5; cyan)[65]. The residue numbering corresponds to the 441-aa human tau isoform, in which the R2 repeat (residues 275–305) is absent. The similarity was again low, with an RMSD of 3.87

398 Å over 42 residues (Fig. 6b).

399 Likewise, comparison with AD-derived PHFs (PDB 6HRE; cyan) [66] showed
400 similarity only in a short loop near S320 (RMSD = 2.09 Å over 16 residues), whereas the
401 overall fold was clearly distinct (Fig. 6c). Taken together, the fold obtained here is distinct
402 from previously reported tau filament structures, including the Pick fold, the three-lobed
403 fold, nor the Alzheimer PHF fold. Importantly, it also differs from the patient-derived
404 P301L fold, suggesting that the combination of P301L and S320F mutations stabilizes a
405 novel filament conformation not observed in any previously described human tauopathy.

406

407 **Discussion**

408 P301L/S320F double-mutant has already been established as a rapidly
409 developing tauopathy model characterized by aggregation of and accumulation of
410 phosphorylated tau in neuronal cells, NFT pathology, cognitive impairment, synaptic
411 protein abnormalities, and deficits in contextual memory [27]. In contrast, conventional
412 tau transgenic mice typically require more than 6 months to develop detectable tau tangles.
413 Therefore, AAV-mediated expression of P301L/S320F double-mutant tau can be regarded
414 as a much more robust model of tau pathology. We further demonstrate that peripheral
415 administration of the recombinant AAV-PHP.eB encoding P301L/S320F mutant tau
416 rapidly induced the neuronal intracellular aggregation and filament formation in mouse
417 brains without the injection of exogenous seeds to mouse brains. Owing to this
418 combination of mutations, P301L/S320F double-mutant tau provides an excellent and not
419 highly invasive tauopathy model in which tau pathology is markedly accelerated

420 following AAV delivery.

421 Our cryo-EM analysis revealed that the extracted filaments consisted
422 predominantly of single helical filaments, and the final reconstructed map reached a
423 resolution of 2.2 Å. The ordered core was composed of tau residues 279–329, in which
424 five β-sheets connected by loop and turn structures formed a compact three-folded
425 architecture. This fold accounted for 55.9% of all tau filaments with clearly resolved β-
426 sheets observed by cryo-EM. All filaments in which a defined helical pitch could be
427 confidently determined exhibited the structure (Fig. 5). The remaining 44.1 % of
428 filaments displayed a longer helical pitch or non-helical and disordered β-sheets, making
429 structural determination difficult. The fold observed for P301L/S320F mutant tau in this
430 study is distinct from the known tau folds reported in AD and PiD, nor from the structure
431 derived from P301L patient brains (Fig. 6). This indicates that the combination of P301L
432 and S320F generates a newly stabilized and unique three-dimensional conformation.
433 Such structural insights provide important clues for understanding the diversity of tau
434 filaments and the molecular basis of filament formation in tauopathies.

435 The S320F mutation is clinically associated with pathology resembling sporadic
436 PiD, in which both straight and twisted tau filaments have been reported. However,
437 whereas PiD inclusions are composed exclusively of 3R tau, the insoluble tau fraction
438 from S320F carriers contains both 3R and 4R tau isoforms [25]. Although S320F carriers
439 exhibit PiD-like straight filament formation and develop frontotemporal dementia, the
440 coexistence of 3R and 4R tau suggests that the underlying filament architecture in these
441 cases may differ from that of typical PiD, which is defined by the exclusive presence of
442 3R tau. Electron microscopy has further shown that the major tau species (~80%) form

443 straight filaments similar to those in AD [25,67]. *In vitro*, S320F tau has been shown to
444 increase the rate of tau nucleation, shorten the lag phase of aggregation, and promote the
445 formation of short protofibrils and oligomers [68,69], which may explain the ability of
446 this mutant to aggregate in the absence of preformed seeds [70]. Taking these previous
447 reports together with our structural data, S320F appears to form a stable loop through π–
448 π stacking between F320 aromatic rings along the Z-axis and hydrophobic interactions
449 with the surrounding residues Q307, V309, P312, L315, and V318. Because Q307, V309,
450 P312, L315, and V318 are shared by both 3R and 4R tau, tau carrying the S320F mutation
451 is likely to recruit both free 3R and 4R tau into the growing filaments. Thus, the loop
452 structure centered on S320F may accelerate amyloid assembly and core formation,
453 providing a mechanistic explanation for the presence of both 3R and 4R isoforms in the
454 insoluble tau fractions from S320F carriers. Furthermore, comparison of the S320F-
455 containing loop with the structure of tau filaments from PiD patients lacking this mutation
456 reveals similarities in the length and packing of the major hairpin-like arm around
457 residues 306–341 and in the packing of residues near position 320. Taken together, these
458 observations suggest that the S320F mutation itself, rather than tau isoform composition
459 alone, may contribute to the emergence of a PiD-like disease phenotype through its
460 unique structural effects, even in filaments containing both 3R and 4R tau isoforms.

461 However, among filaments with a clearly defined pitch, we did not observe a
462 robust fold that incorporated WT 3R or 4R tau. Such species likely belong to the
463 population of filaments with excessively long pitch and partially ordered β-sheets in
464 which structural determination was not feasible. This implies that, although S320F
465 promotes filament formation through loop stabilization, it may not by itself be sufficient

466 to generate highly ordered β-sheets within a short time frame in the model mouse. This
467 interpretation is consistent with previous observations that AAV-mediated expression of
468 S320F alone in neonatal ventricles does not produce substantial tau aggregation within
469 three months [27].

470 In the present study, the combination of P301L and S320F mutations generated
471 not only the S320F-dependent loop but also an additional hydrophobic interaction
472 between L301 and I328. This hydrophobic contact appears to rigidify the base of the
473 S320F-dependent loop, thereby defining a specific loop spanning 28 amino acids from
474 L301 to I328. Formation of this L301–I328 loop exposes the hydrophobic residues V306
475 and I308 on the outer surface of the loop, allowing L282, L284, V287, and Q288 to pack
476 against them and stabilize the three-folded architecture. Furthermore, interactions
477 between N286 and S289 are likely to support and lock in this folding pattern. Collectively,
478 these interactions contribute to the robust, compact three-folded structure observed for
479 P301L/S320F double-mutant tau.

480 One of the key advantages of our model is the rapid induction of tau pathology.
481 Whereas conventional models such as PS19 mice require more than 6 months for
482 detectable tau aggregation, our system recapitulated tau accumulation and filament
483 formation within 1–2 months. This should not be interpreted as a more faithful
484 reproduction of human pathology, but rather as a powerful experimental system that
485 enables rapid induction and analysis of tau aggregation. Because tau filament formation
486 in our model was induced within at most 2 months in mouse brains, it is plausible that we
487 captured a particularly stable and compact fold. WT 4R tau does not contain L301, and
488 3R tau lacks this region entirely; therefore, filaments that incorporate WT tau isoforms

489 are expected to adopt structures distinct from the fold identified here, and their maturation
490 may require longer periods. Long-term observation will thus be necessary to elucidate
491 how WT tau is incorporated and how these filaments structurally evolve.

492 This study has several limitations: although peripheral administration of a
493 recombinant AAV-PHP.eB achieved widespread gene delivery throughout the brain,
494 transduction efficiency varied among regions, and the distribution of tau aggregates
495 largely mirrored the pattern of AAV infection. In addition, because the number of
496 transduced cells was limited, we did not observe large-scale neurodegeneration such as
497 overt brain atrophy or extensive neuronal loss. Future studies combining region-specific
498 intracranial injections with strategies to further enhance transduction efficiency may
499 allow stronger pathology and more widespread neurodegeneration to be modeled.

500 Taken together, our findings demonstrate that P301L/S320F mutant tau promotes
501 aggregation and filament formation in the absence of exogenous seeds, and that the
502 resulting fold is clearly distinct from previously reported tau structures. These results
503 deepen our mechanistic understanding of tau aggregation and provide a structural
504 framework for exploring the basis of tauopathies and for identifying potential therapeutic
505 targets.

506

507 **Conclusions**

508 In this study, we established a non-invasive and rapid *in vivo* model of tau
509 pathology by administering a recombinant AAV-PHP.eB from the periphery. Expression
510 of the P301L/S320F double-mutant human tau in adult mouse brain induced robust tau

511 aggregation without the need for exogenous seeds, accompanied by phosphorylation
512 patterns commonly observed in AD, including AT8, AT180, pSer396, and PHF-1. The
513 concomitant detection of early (AT8 and AT180) and late (pSer396 and PHF-1)
514 phosphorylation epitopes indicates that tau phosphorylation progresses in a stepwise
515 manner, leading to the accumulation of filamentous tau species that have reached an
516 advanced pathological maturation stage. Our cryo-EM analysis of sarkosyl-insoluble tau
517 filaments demonstrated that the combined P301L and S320F mutations cooperatively
518 remodel the tau core to generate a previously unreported filament fold distinct from
519 known patient-derived structures. Together, these findings reveal the strong intrinsic
520 aggregation propensity and unique fibrillization mechanism of P301L/S320F tau *in vivo*.
521 The model presented here faithfully reproduces tau pathology on a background of
522 humanized tau and Aβ deposition, providing a powerful platform for dissecting disease
523 mechanisms and advancing therapeutic strategies for tauopathies.

524 **Abbreviations**

525 AAV: adeno-associated virus

526 AD: Alzheimer disease

527 APP: amyloid precursor protein

528 BS cells: biosensor cells

529 CA2: Cornu Ammonis 2

530 CFP: cyan fluorescent protein

531 cryo-EM: cryo-electron microscopy

532 DAPI: 4',6-diamidino-2-phenylindole

533 EM: electron microscopy

534 FRET: fluorescence resonance energy transfer

535 FTD: frontotemporal dementia

536 FTDP-17: frontotemporal dementia with Parkinsonism linked to chromosome 17

537 HEK293A: human embryonic kidney 293A

538 hMAPT: human microtubule-associated protein tau

539 MPtA: medial parietal association area

540 PBS: phosphate-buffered saline

541 RD: repeat domain (tau)

542 Sup: sarkosyl-soluble fraction

543 Pellet: sarkosyl-insoluble fraction

544 vg: viral genomes

545 WPRE: woodchuck hepatitis virus post-transcriptional regulatory element

546 WT: wild-type

547

548 **Figure Legends**

549 **Figure 1. P301L/S320F double-mutant tau forms sarkosyl-insoluble tau filaments in cultured**
550 **cells.**

551 **a**. Schematic representation of human 1N4R tau, showing the amino acid sequences of
552 the microtubule-binding repeats (R1–R4), and the mutation sites P301L and S320F.

553 **b**. Experimental design for assessing tau aggregation in HEK293A cells. Cells stably
554 expressing 1N3R and 1N4R WT tau isoforms were transfected with plasmids encoding
555 either 1N4R WT tau or 1N4R P301L/S320F double-mutant tau, followed by sarkosyl
556 extraction to separate the soluble (Sup) and insoluble (Pellet) fractions.

557 **c**. Western blot analysis of each fraction. Tau in the sarkosyl-insoluble fraction was
558 prominently detected in the P301L/S320F group compared with the WT and empty-vector
559 (EV) groups. GAPDH served as a loading control.

560 **d**. Quantification of sarkosyl-insoluble tau normalized to soluble tau (mean ± SEM; n =
561 3 per group). Statistical significance was evaluated using a two-tailed Welch's t-test. For
562 all comparisons: $p < 0.05$ (*), ns = not significant.

563 **e**. Resuspended sarkosyl-insoluble pellets obtained as in b were negatively stained with
564 2% phosphotungstic acid (pH 7.0) and observed under a transmission electron microscope.
565 Scale bar is 100 nm.

566

567 **Figure 2. P301L/S320F tau induces phosphorylated tau aggregates in the brains of *App*$^{NL-G-}$**
568 **^{F}/*hMAPT* mice.**

569 **a.** Experimental design. *App*$^{NL-G-F}$/*hMAPT* double knock-in mice aged 9–11 months were
570 intravenously injected via the retro-orbital sinus with the recombinant AAV-PHP.eB
571 (2×10^{11}vg/mouse). Brains were collected 2 months after injection for histological analysis.

572 **b**. Immunostaining of brain hemispheres with AT8 antibody in mice expressing WT tau
573 or P301L/S320F via AAV-PHP.eB, and from non-injected control mice.

574 **c**. High-magnification images of the MPtA (boxed by a solid line) in b. Scale bars are 100
575 mm.

576 **d.** Quantification of AT8-positive area in the MPtA. Statistical significance was
577 determined by Welch's two-tailed *t*-test. Mean ± SEM, n = 3. *$p < 0.05$, ns = not
578 significant.

579 **e**. High-magnification images of the hippocampal CA2 region in b. Scale bars are 100
580 mm.

581 **f**. Quantification of AT8-positive area in the CA2 region. Statistical significance was
582 determined by Welch's two-tailed *t*-test. Mean ± SEM, n = 3. *$p < 0.05$, ns = not
583 significant.

584

585 **Figure 3. Evaluation of tau aggregation propensity and seeding activity in mouse brains**
586 **expressing P301L/S320F tau**

587 **a**. Experimental workflow. Following systemic administration of AAV-PHP.eB encoding

588 either WT or P301L/S320F tau, mouse brain hemispheres were fractionated into soluble
589 (Sup) and insoluble (Pellet) fractions by the sarkosyl extraction method.

590 **b**. Western blot analysis of each fraction.

591 **c**. Ratio of sarkosyl-insoluble to soluble tau (mean ± SEM; n = 3 per group), showing a
592 significant increase in the P301L/S320F group ($p < 0.05$). Statistical significance was
593 determined by Welch's two-tailed *t*-test.

594 **d**. Sarkosyl-insoluble pellets were negatively stained with 2% phosphotungstic acid (pH
595 7.0).

596 **e**-**g**. Filaments positive for TauC4 (e), AT8 (f), and pS396 (g) antibodies were observed
597 in the P301L/S320F group. Secondary antibodies used were 10 nm gold-conjugated anti-
598 rabbit IgG for TauC4 and pS396 and 5 nm gold-conjugated anti-mouse IgG for AT8.

599

600 **Figure 4. Cryo-EM structure of P301L/S320F tau filaments extracted from mouse brains.**

601 **a.** Representative cross-sections through the cryo-EM reconstruction of P301L/S320F tau
602 filaments, shown perpendicular to the helical axis with a projected thickness of
603 approximately one rung. The map resolution is 2.24 Å. Scale bar is 5 nm.

604 **b**. Three-dimensional reconstruction of the P301L/S320F tau filaments obtained by
605 helical reconstruction. Scale bar is 5 nm.

606 **c**. Amino acid sequence of human 1N4R tau (residues 255–367) corresponding to the
607 reconstructed region. The five β-strand regions (β1–β5) are indicated by green arrows.
608 Mutation sites P301L and S320F are shown in red.

609 **d**. Rendered view of the secondary structure elements in two successive rungs.

610

611 **Figure 5. Local structural effects of P301L and S320F mutations on tau filaments.**

612 **a**. Sharpened cryo-EM density map of the P301L/S320F tau filament with the atomic
613 model fitted. Major side chains are shown, and mutated residues L301 and F320 are
614 highlighted in red.

615 **b**. Schematic representation of the P301L/S320F tau filament fold. β-strands are indicated
616 by thick lines with arrowheads. Orange semicircles indicate additional densities observed
617 near the filament crossover region.

618 **c**. Structure surrounding the P301L mutation site. The L301 residue (red) is positioned
619 within the β-strand core and forms hydrophobic interactions with nearby residues,
620 including V300 and I297.

621 **d**. Structure surrounding the S320F mutation site. The F320 residue (red) is embedded
622 within the loop region and forms hydrophobic interactions with Q307, V309, P312, L315,
623 and V318, which likely contribute to the stabilization of the filament.

624

625 **Figure 6. Comparison with previously reported patient-derived tau filament structures.**

626 **a**. Structural comparison between P301L/S320F mouse tau filaments (magenta) and
627 P301L patient tau filaments (cyan, PDB: 9GG0), with an RMSD of 4.23 Å over 40
628 residues.

629 **b**. Structural comparison between P301L/S320F mouse tau filaments (magenta) and PiD

630 patient tau filaments (cyan, PDB: 6GX5), with an RMSD of 3.87 Å over 42 residues.

631 **c**. Structural comparison between P301L/S320F mouse tau filaments (magenta) and AD

632 patient tau filaments (cyan, PDB: 6HRE), with an RMSD of 2.09 Å over 16 residues.

633

Declarations

Ethics approval and consent to participate

All animal experiments were conducted in accordance with the guidelines of the Institutional Animal Care Committee of the Graduate School of Pharmaceutical Sciences at the University of Tokyo (protocol no. P3-20).

Consent for publication

Not applicable.

Availability of data and materials

Cryo-EM maps have been deposited in the Electron Microscopy Data Bank (EMDB) with the accession numbers EMD-68389 (P301L/S320F tau filament). Corresponding refined atomic models have been deposited in the Protein Data Bank (PDB) under accession numbers PDB: 22JY. The datasets used and analyzed during the current study are available from the corresponding author on reasonable request.

Competing interests

The authors declare that they have no competing interests.

Funding

This work was supported by the Research Support Project for Life Science and Drug Discovery (Basis for Supporting Innovative Drug Discovery and Life Science Research (BINDS)) from the Japan Agency for Medical Research and Development (AMED) under Grant Number JP23dm0207073 (for T.T.), JP24wm0625303 (for T.T.), Moonshot Research and Development Program (JPMJMS2024-1 for T.T.) from the Japan Science and Technology Agency (JST), KAKENHI (JP25KJ1009 for M.Ka., JP23H00394 for T.T., JP23K06112 for T.K.) from the Japan Society for the Promotion of Science (JSPS), and the International Graduate Program of Innovation for Intelligent World (GCL/IIW for M.Ka.) from the University of Tokyo.

Authors' contributions

M.Ka performed cell and biochemical experiments, extracted filaments from mouse brains, analyzed the data, prepared figures, and wrote the original draft of the manuscript. T.K. supervised the biochemical experiments and provided technical guidance. H.Y. conducted cryo-EM imaging, performed structural reconstruction, and assisted in figure preparation. L.T. contributed to the optimization of experimental conditions for cell-based and mouse experiments. K.Y. performed immunohistochemical staining of mouse brain sections. A.S. carried out quantitative analyses of Western blot and immunohistochemical staining data. X.L. extracted tau filaments from cultured cells. S.T. constructed the P301L/S320F tau plasmid and established the AAV-PHP.eB systemic delivery protocol in mice. T.C.S. and T.S. established and provided *App*$^{NL\text{-}G\text{-}F}$*/hMAPT*

675 double knock-in mice. M.Ki supervised the structural analysis and provided critical input
676 on the manuscript. T.T. conceived and supervised the overall project, secured funding,
677 and served as the corresponding author.

678

679 **Acknowledgements**

680 AAV production and purification were performed by the Department of
681 Neurophysiology & Neural Repair, Gunma University Graduate School of Medicine,
682 Gunma University (supported by JP21dm0207111). The authors are grateful to the
683 Feinstein Institutes for Medical Research (Dr. Philippe Marambaud and Dr. Jeremy
684 Koppel) for providing the PHF-1 antibody, originally developed by Dr. Peter Davies at
685 Albert Einstein College of Medicine [71]. We acknowledge Viviana Gradinaru and
686 Benjamin Deverman for their pioneering work in developing the AAV-PHP.eB capsid [42].

687

688 **References**

689 1. Goedert M, Spillantini MG, Jakes R, Rutherford D, Crowther RA. Multiple isoforms
690 of human microtubule-associated protein tau: sequences and localization in
691 neurofibrillary tangles of Alzheimer's disease. Neuron. 1989;3:519–26.
692 https://doi.org/10.1016/0896-6273(89)90210-9

693 2. Kimura T, Sato H, Kano M, Tatsumi L, Tomita T. Novel aspects of the
694 phosphorylation and structure of pathological tau: implications for tauopathy
695 biomarkers. FEBS Open Bio. 2024;14:181–93. https://doi.org/10.1002/2211-
696 5463.13667

697 3. McMillan P, Korvatska E, Poorkaj P, Evstafjeva Z, Robinson L, Greenup L, et al. Tau
698 isoform regulation is region and cell-specific in mouse brain. J Comp Neurol.
699 2008;511:788–803. https://doi.org/10.1002/cne.21867

700 4. Gustke N, Steiner B, Mandelkow E-M, Biernat J, Meyer H e., Goedert M, et al. The
701 Alzheimer-like phosphorylation of tau protein reduces microtubule binding and
702 involves Ser-Pro and Thr-Pro motifs. FEBS Lett. 1992;307:199–205.
703 https://doi.org/10.1016/0014-5793(92)80767-B

704 5. Poorkaj P, Bird TD, Wijsman E, Nemens E, Garruto RM, Anderson L, et al. Tau is a
705 candidate gene for chromosome 17 frontotemporal dementia. Ann Neurol.
706 1998;43:815–25. https://doi.org/10.1002/ana.410430617

707 6. Hutton M, Lendon CL, Rizzu P, Baker M, Froelich S, Houlden H, et al. Association
708 of missense and 5′-splice-site mutations in tau with the inherited dementia FTDP-17.
709 Nature. Nature Publishing Group; 1998;393:702–5. https://doi.org/10.1038/31508

710 7. Goedert M, Spillantini MG, Cairns NJ, Crowther RA. Tau proteins of alzheimer
711 paired helical filaments: Abnormal phosphorylation of all six brain isoforms. Neuron.
712 1992;8:159–68. https://doi.org/10.1016/0896-6273(92)90117-V

713 8. Fitzpatrick AWP, Falcon B, He S, Murzin AG, Murshudov G, Garringer HJ, et al.
714 Cryo-EM structures of tau filaments from Alzheimer's disease. Nature. Nature
715 Publishing Group; 2017;547:185–90. https://doi.org/10.1038/nature23002

716 9. Scheres SH, Zhang W, Falcon B, Goedert M. Cryo-EM structures of tau filaments.

717 Curr Opin Struct Biol. 2020;64:17–25. https://doi.org/10.1016/j.sbi.2020.05.011

718 10. Shi Y, Zhang W, Yang Y, Murzin AG, Falcon B, Kotecha A, et al. Structure-based
719 classification of tauopathies. Nature. Nature Publishing Group; 2021;598:359–63.
720 https://doi.org/10.1038/s41586-021-03911-7

721 11. Braak H, Braak E. Neuropathological stageing of Alzheimer-related changes. Acta
722 Neuropathol (Berl). 1991;82:239–59. https://doi.org/10.1007/BF00308809

723 12. Arriagada PV, Growdon JH, Hedley-Whyte ET, Hyman BT. Neurofibrillary tangles
724 but not senile plaques parallel duration and severity of Alzheimer's disease.
725 Neurology. Wolters Kluwer; 1992;42:631–631.
726 https://doi.org/10.1212/WNL.42.3.631

727 13. Morishima-Kawashima M, Hasegawa M, Takio K, Suzuki M, Titani K, Ihara Y.
728 Ubiquitin is conjugated with amino-terminally processed tau in paired helical
729 filaments. Neuron. 1993;10:1151–60. https://doi.org/10.1016/0896-6273(93)90063-w

730 14. Dale GE, Leigh PN, Luthert P, Anderton BH, Roberts GW. Neurofibrillary tangles in
731 dementia pugilistica are ubiquitinated. J Neurol Neurosurg Psychiatry. BMJ
732 Publishing Group Ltd; 1991;54:116–8. https://doi.org/10.1136/jnnp.54.2.116

733 15. Cripps D, Thomas SN, Jeng Y, Yang F, Davies P, Yang AJ. Alzheimer disease-
734 specific conformation of hyperphosphorylated paired helical filament-Tau is
735 polyubiquitinated through Lys-48, Lys-11, and Lys-6 ubiquitin conjugation. J Biol
736 Chem. 2006;281:10825–38. https://doi.org/10.1074/jbc.M512786200

737 16. Cohen TJ, Guo JL, Hurtado DE, Kwong LK, Mills IP, Trojanowski JQ, et al. The
738 acetylation of tau inhibits its function and promotes pathological tau aggregation. Nat
739 Commun. 2011;2:252. https://doi.org/10.1038/ncomms1255

740 17. Cook C, Carlomagno Y, Gendron TF, Dunmore J, Scheffel K, Stetler C, et al.
741 Acetylation of the KXGS motifs in tau is a critical determinant in modulation of tau
742 aggregation and clearance. Hum Mol Genet. 2014;23:104–16.
743 https://doi.org/10.1093/hmg/ddt402

744 18. Dorval V, Fraser PE. Small Ubiquitin-like Modifier (SUMO) Modification of
745 Natively Unfolded Proteins Tau and α-Synuclein *. J Biol Chem. Elsevier;

2006;281:9919–24. https://doi.org/10.1074/jbc.M510127200

19. Yokoyama M, Kobayashi H, Tatsumi L, Tomita T. Mouse Models of Alzheimer's Disease. Front Mol Neurosci [Internet]. Frontiers; 2022 [cited 2025 June 26];15. https://doi.org/10.3389/fnmol.2022.912995

20. Clavaguera F, Akatsu H, Fraser G, Crowther RA, Frank S, Hench J, et al. Brain homogenates from human tauopathies induce tau inclusions in mouse brain. Proc Natl Acad Sci. Proceedings of the National Academy of Sciences; 2013;110:9535–40. https://doi.org/10.1073/pnas.1301175110

21. Iba M, Guo JL, McBride JD, Zhang B, Trojanowski JQ, Lee VM-Y. Synthetic Tau Fibrils Mediate Transmission of Neurofibrillary Tangles in a Transgenic Mouse Model of Alzheimer's-Like Tauopathy. J Neurosci. Society for Neuroscience; 2013;33:1024–37. https://doi.org/10.1523/JNEUROSCI.2642-12.2013

22. Peeraer E, Bottelbergs A, Van Kolen K, Stancu I-C, Vasconcelos B, Mahieu M, et al. Intracerebral injection of preformed synthetic tau fibrils initiates widespread tauopathy and neuronal loss in the brains of tau transgenic mice. Neurobiol Dis. 2015;73:83–95. https://doi.org/10.1016/j.nbd.2014.08.032

23. Terwel D, Lasrado R, Snauwaert J, Vandeweert E, Van Haesendonck C, Borghgraef P, et al. Changed Conformation of Mutant Tau-P301L Underlies the Moribund Tauopathy, Absent in Progressive, Nonlethal Axonopathy of Tau-4R/2N Transgenic Mice*. J Biol Chem. 2005;280:3963–73. https://doi.org/10.1074/jbc.M409876200

24. Wang K-W, Zhang G, Kuo M-H. Frontotemporal Dementia P301L Mutation Potentiates but Is Not Sufficient to Cause the Formation of Cytotoxic Fibrils of Tau. Int J Mol Sci. Multidisciplinary Digital Publishing Institute; 2023;24:14996. https://doi.org/10.3390/ijms241914996

25. Rosso SM, Van Herpen E, Deelen W, Kamphorst W, Severijnen L-A, Willemsen R, et al. A novel tau mutation, S320F, causes a tauopathy with inclusions similar to those in Pick's disease. Ann Neurol. 2002;51:373–6. https://doi.org/10.1002/ana.10140

26. Chen D, Bali S, Singh R, Wosztyl A, Mullapudi V, Vaquer-Alicea J, et al. FTD-tau S320F mutation stabilizes local structure and allosterically promotes amyloid motif-

776 dependent aggregation. Nat Commun. 2023;14:1625. https://doi.org/10.1038/s41467-
777 023-37274-6

778 27. Koller EJ, Gonzalez De La Cruz E, Machula T, Ibanez KR, Lin W-L, Williams T, et
779 al. Combining P301L and S320F tau variants produces a novel accelerated model of
780 tauopathy. Hum Mol Genet. 2019;28:3255–69. https://doi.org/10.1093/hmg/ddz151

781 28. Deverman BE, Pravdo PL, Simpson BP, Kumar SR, Chan KY, Banerjee A, et al.
782 Cre-dependent selection yields AAV variants for widespread gene transfer to the
783 adult brain. Nat Biotechnol. Nature Publishing Group; 2016;34:204–9.
784 https://doi.org/10.1038/nbt.3440

785 29. Challis RC, Ravindra Kumar S, Chan KY, Challis C, Beadle K, Jang MJ, et al.
786 Systemic AAV vectors for widespread and targeted gene delivery in rodents. Nat
787 Protoc. Nature Publishing Group; 2019;14:379–414. https://doi.org/10.1038/s41596-
788 018-0097-3

789 30. Saito T, Mihira N, Matsuba Y, Sasaguri H, Hashimoto S, Narasimhan S, et al.
790 Humanization of the entire murine Mapt gene provides a murine model of
791 pathological human tau propagation. J Biol Chem. 2019;294:12754–65.
792 https://doi.org/10.1074/jbc.RA119.009487

793 31. Liu F, Gong C-X. Tau exon 10 alternative splicing and tauopathies. Mol
794 Neurodegener. 2008;3:8. https://doi.org/10.1186/1750-1326-3-8

795 32. Saito T, Matsuba Y, Mihira N, Takano J, Nilsson P, Itohara S, et al. Single App
796 knock-in mouse models of Alzheimer's disease. Nat Neurosci. Nature Publishing
797 Group; 2014;17:661–3. https://doi.org/10.1038/nn.3697

798 33. Cai T, Morishima K, Takagi-Niidome S, Tominaga A, Tomita T. Conformational
799 Dynamics of Transmembrane Domain 3 of Presenilin 1 Is Associated with the
800 Trimming Activity of γ-Secretase. J Neurosci Off J Soc Neurosci. 2019;39:8600–10.
801 https://doi.org/10.1523/JNEUROSCI.0838-19.2019

802 34. Araki M, Ito K, Takatori S, Ito G, Tomita T. BORCS6 is involved in the enlargement
803 of lung lamellar bodies in Lrrk2 knockout mice. Hum Mol Genet. 2021;30:1618–31.
804 https://doi.org/10.1093/hmg/ddab146

35. Tomita T, Maruyama K, Saido TC, Kume H, Shinozaki K, Tokuhiro S, et al. The presenilin 2 mutation (N141I) linked to familial Alzheimer disease (Volga German families) increases the secretion of amyloid beta protein ending at the 42nd (or 43rd) residue. Proc Natl Acad Sci U S A. 1997;94:2025–30. https://doi.org/10.1073/pnas.94.5.2025

36. Kanatsu K, Morohashi Y, Suzuki M, Kuroda H, Watanabe T, Tomita T, et al. Decreased CALM expression reduces Aβ42 to total Aβ ratio through clathrin-mediated endocytosis of γ-secretase. Nat Commun. 2014;5:3386. https://doi.org/10.1038/ncomms4386

37. Lee VM, Balin BJ, Otvos L, Trojanowski JQ. A68: a major subunit of paired helical filaments and derivatized forms of normal Tau. Science. 1991;251:675–8. https://doi.org/10.1126/science.1899488

38. Lövestam S, Schweighauser M, Matsubara T, Murayama S, Tomita T, Ando T, et al. Seeded assembly in vitro does not replicate the structures of α-synuclein filaments from multiple system atrophy. FEBS Open Bio. 2021;11:999–1013. https://doi.org/10.1002/2211-5463.13110

39. Tarutani A, Miyata H, Nonaka T, Hasegawa K, Yoshida M, Saito Y, et al. Human tauopathy-derived tau strains determine the substrates recruited for templated amplification. Brain J Neurol. 2021;144:2333–48. https://doi.org/10.1093/brain/awab091

40. Holmes BB, Furman JL, Mahan TE, Yamasaki TR, Mirbaha H, Eades WC, et al. Proteopathic tau seeding predicts tauopathy in vivo. Proc Natl Acad Sci U S A. 2014;111:E4376-4385. https://doi.org/10.1073/pnas.1411649111

41. Tarutani A, Lövestam S, Zhang X, Kotecha A, Robinson AC, Mann DMA, et al. Cryo-EM structures of tau filaments from SH-SY5Y cells seeded with brain extracts from cases of Alzheimer's disease and corticobasal degeneration. FEBS Open Bio. 2023;13:1394–404. https://doi.org/10.1002/2211-5463.13657

42. Chan KY, Jang MJ, Yoo BB, Greenbaum A, Ravi N, Wu W-L, et al. Engineered AAVs for efficient noninvasive gene delivery to the central and peripheral nervous systems. Nat Neurosci. 2017;20:1172–9. https://doi.org/10.1038/nn.4593

835 43. Konno A, Hirai H. Efficient whole brain transduction by systemic infusion of
836 minimally purified AAV-PHP.eB. J Neurosci Methods. 2020;346:108914.
837 https://doi.org/10.1016/j.jneumeth.2020.108914

838 44. Shinohara Y, Konno A, Nitta K, Matsuzaki Y, Yasui H, Suwa J, et al. Effects of
839 Neutralizing Antibody Production on AAV-PHP.B-Mediated Transduction of the
840 Mouse Central Nervous System. Mol Neurobiol. 2019;56:4203–14.
841 https://doi.org/10.1007/s12035-018-1366-4

842 45. Iguchi A, Takatori S, Kimura S, Muneto H, Wang K, Etani H, et al. INPP5D
843 modulates TREM2 loss-of-function phenotypes in a β-amyloidosis mouse model.
844 iScience. 2023;26:106375. https://doi.org/10.1016/j.isci.2023.106375

845 46. Kimura T, Hosokawa T, Taoka M, Tsutsumi K, Ando K, Ishiguro K, et al.
846 Quantitative and combinatory determination of in situ phosphorylation of tau and its
847 FTDP-17 mutants. Sci Rep. Nature Publishing Group; 2016;6:33479.
848 https://doi.org/10.1038/srep33479

849 47. Yadav S, Vinothkumar KR. Factors affecting macromolecule orientations in thin
850 films formed in cryo-EM. Acta Crystallogr Sect Struct Biol. 2024;80:535–50.
851 https://doi.org/10.1107/S2059798324005229

852 48. Schorb M, Haberbosch I, Hagen WJH, Schwab Y, Mastronarde DN. Software tools
853 for automated transmission electron microscopy. Nat Methods. Nature Publishing
854 Group; 2019;16:471–7. https://doi.org/10.1038/s41592-019-0396-9

855 49. Punjani A, Rubinstein JL, Fleet DJ, Brubaker MA. cryoSPARC: algorithms for rapid
856 unsupervised cryo-EM structure determination. Nat Methods. Nature Publishing
857 Group; 2017;14:290–6. https://doi.org/10.1038/nmeth.4169

858 50. Scheres SHW. Amyloid structure determination in RELION-3.1. Acta Crystallogr
859 Sect Struct Biol. International Union of Crystallography; 2020;76:94–101.
860 https://doi.org/10.1107/S2059798319016577

861 51. Asarnow D, Palovcak E, Cheng Y. UCSF pyem v0.5 [Internet]. 2019.
862 https://doi.org/10.5281/zenodo.3576630

863 52. He S, Scheres SHW. Helical reconstruction in RELION. J Struct Biol.

2017;198:163–76. https://doi.org/10.1016/j.jsb.2017.02.003

53. Jamali K, Käll L, Zhang R, Brown A, Kimanius D, Scheres SHW. Automated model building and protein identification in cryo-EM maps. Nature. Nature Publishing Group; 2024;628:450–7. https://doi.org/10.1038/s41586-024-07215-4

54. Emsley P, Cowtan K. Coot: model-building tools for molecular graphics. Acta Crystallogr D Biol Crystallogr. International Union of Crystallography; 2004;60:2126–32. https://doi.org/10.1107/S0907444904019158

55. Liebschner D, Afonine PV, Baker ML, Bunkóczi G, Chen VB, Croll TI, et al. Macromolecular structure determination using X-rays, neutrons and electrons: recent developments in Phenix. Acta Crystallogr Sect Struct Biol. International Union of Crystallography; 2019;75:861–77. https://doi.org/10.1107/S2059798319011471

56. Yamashita K, Palmer CM, Burnley T, Murshudov GN. Cryo-EM single-particle structure refinement and map calculation using Servalcat. Acta Crystallogr Sect Struct Biol. International Union of Crystallography; 2021;77:1282–91. https://doi.org/10.1107/S2059798321009475

57. Meng EC, Goddard TD, Pettersen EF, Couch GS, Pearson ZJ, Morris JH, et al. UCSF ChimeraX: Tools for structure building and analysis. Protein Sci. 2023;32:e4792. https://doi.org/10.1002/pro.4792

58. Hoq MR, Fernandez A, Vago FS, Hallinan GI, Bharath SR, Li D, et al. Cryo-EM structures of cotton wool plaques' amyloid β and of tau filaments in dominantly inherited Alzheimer disease. Acta Neuropathol (Berl). 2024;148:20. https://doi.org/10.1007/s00401-024-02786-y

59. Nakane, T. atom2svg [Internet]. 2020. https://doi.org/10.5281/zenodo.4090925

60. Mercken M, Vandermeeren M, Lübke U, Six J, Boons J, Van de Voorde A, et al. Monoclonal antibodies with selective specificity for Alzheimer Tau are directed against phosphatase-sensitive epitopes. Acta Neuropathol (Berl). 1992;84:265–72. https://doi.org/10.1007/BF00227819

61. Goedert M, Jakes R, Crowther RA, Cohen P, Vanmechelen E, Vandermeeren M, et al. Epitope mapping of monoclonal antibodies to the paired helical filaments of

893 Alzheimer's disease: identification of phosphorylation sites in tau protein. Biochem
894 J. 1994;301 (Pt 3):871–7. https://doi.org/10.1042/bj3010871

895 62. Bramblett GT, Goedert M, Jakes R, Merrick SE, Trojanowski JQ, Lee VM.
896 Abnormal tau phosphorylation at Ser396 in Alzheimer's disease recapitulates
897 development and contributes to reduced microtubule binding. Neuron.
898 1993;10:1089–99. https://doi.org/10.1016/0896-6273(93)90057-x

899 63. Schweighauser M, Shi Y, Murzin AG, Garringer HJ, Vidal R, Murrell JR, et al.
900 Distinct tau filament folds in human MAPT mutants P301L and P301T. Nat Struct
901 Mol Biol. 2025;32:1470–8. https://doi.org/10.1038/s41594-025-01575-9

902 64. Heston LL, Mastri AR. Age at Onset of Pick's and Alzheimer's Dementia:
903 Implications for Diagnosis and Research. J Gerontol. 1982;37:422–4.
904 https://doi.org/10.1093/geronj/37.4.422

905 65. Falcon B, Zhang W, Murzin AG, Murshudov G, Garringer HJ, Vidal R, et al.
906 Structures of filaments from Pick's disease reveal a novel tau protein fold. Nature.
907 Nature Publishing Group; 2018;561:137–40. https://doi.org/10.1038/s41586-018-
908 0454-y

909 66. Falcon B, Zhang W, Schweighauser M, Murzin AG, Vidal R, Garringer HJ, et al.
910 Tau filaments from multiple cases of sporadic and inherited Alzheimer's disease
911 adopt a common fold. Acta Neuropathol (Berl). 2018;136:699–708.
912 https://doi.org/10.1007/s00401-018-1914-z

913 67. Rosso SM, Kaat LD, Baks T, Joosse M, de Koning I, Pijnenburg Y, et al.
914 Frontotemporal dementia in The Netherlands: patient characteristics and prevalence
915 estimates from a population-based study. Brain. 2003;126:2016–22.
916 https://doi.org/10.1093/brain/awg204

917 68. Combs B, Gamblin TC. FTDP-17 tau mutations induce distinct effects on
918 aggregation and microtubule interactions. Biochemistry. 2012;51:8597–607.
919 https://doi.org/10.1021/bi3010818

920 69. Bardai FH, Wang L, Mutreja Y, Yenjerla M, Gamblin TC, Feany MB. A Conserved
921 Cytoskeletal Signaling Cascade Mediates Neurotoxicity of FTDP-17 Tau Mutations
922 In Vivo. J Neurosci Off J Soc Neurosci. 2018;38:108–19.

923 https://doi.org/10.1523/JNEUROSCI.1550-17.2017

924 70. Strang KH, Croft CL, Sorrentino ZA, Chakrabarty P, Golde TE, Giasson BI. Distinct
925 differences in prion-like seeding and aggregation between Tau protein variants
926 provide mechanistic insights into tauopathies. J Biol Chem. 2018;293:2408–21.
927 https://doi.org/10.1074/jbc.M117.815357

928 71. Greenberg SG, Davies P, Schein JD, Binder LI. Hydrofluoric acid-treated tau PHF
929 proteins display the same biochemical properties as normal tau. J Biol Chem.
930 1992;267:564–9. https://doi.org/10.1016/S0021-9258(18)48531-6

931

932

933 **Figures**

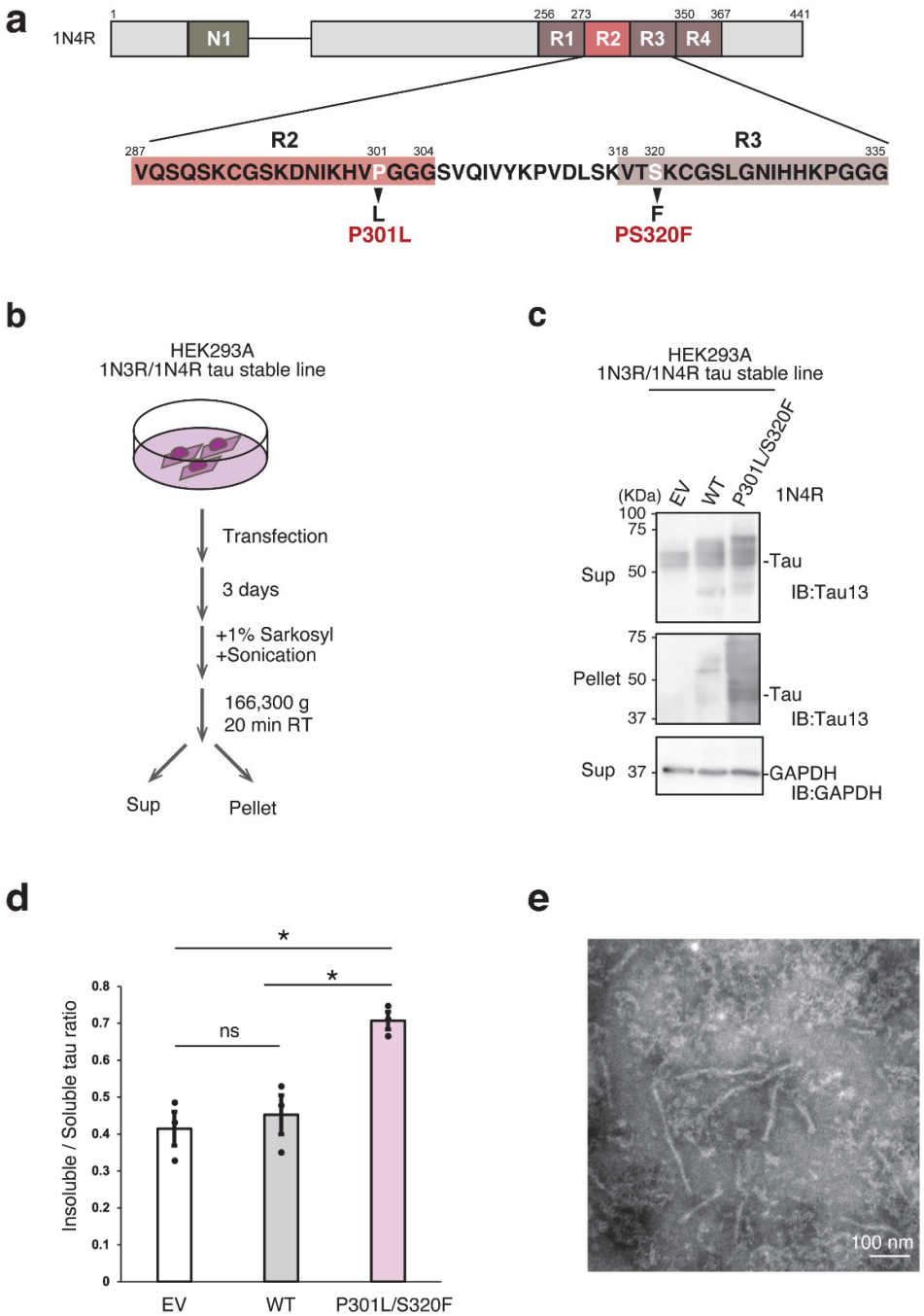

934

935 **Fig. 1**

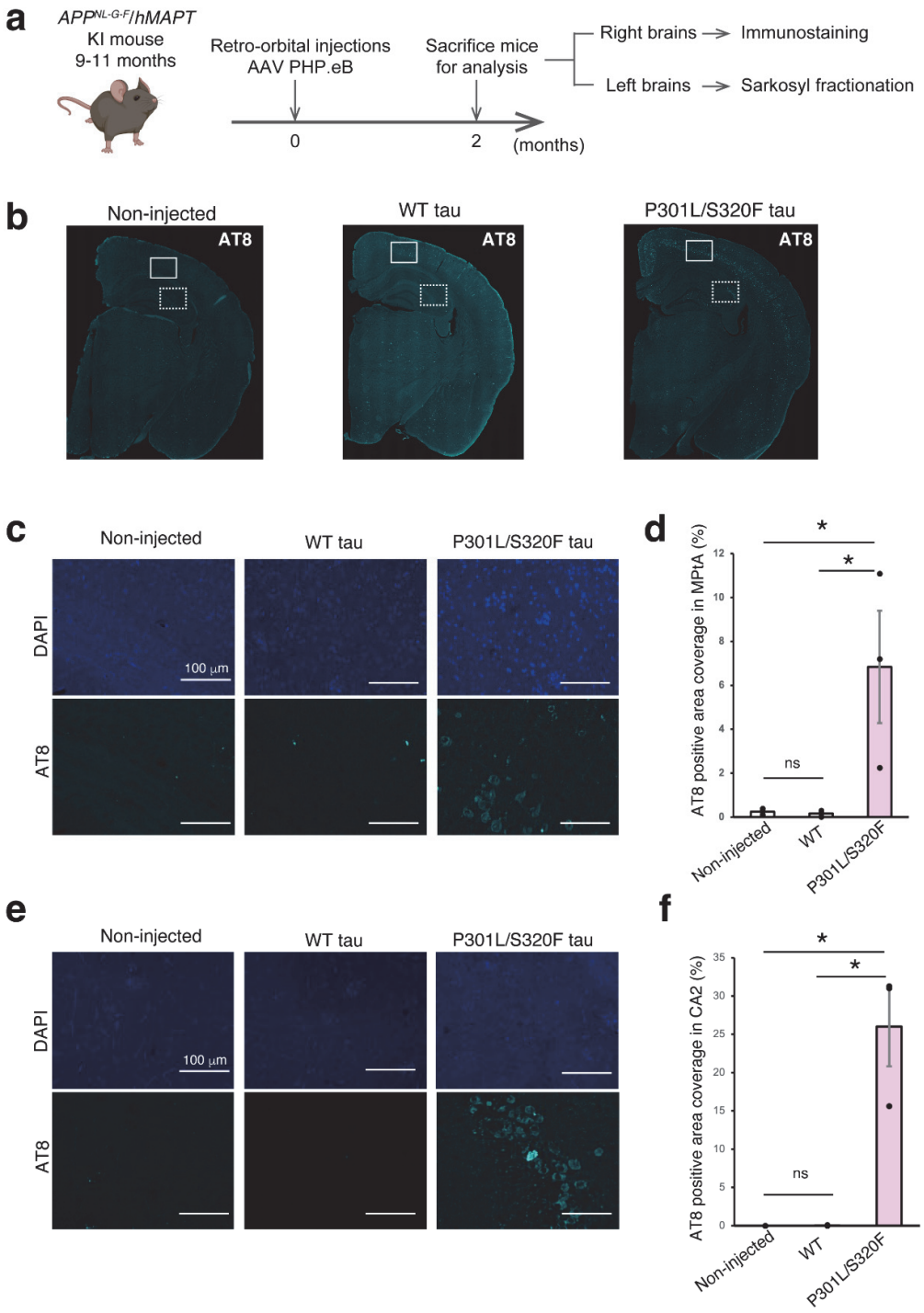
a
APPNL-G-F/hMAPT
KI mouse
9-11 months
Retro-orbital injections
AAV PHP.eB
Sacrifice mice
for analysis
Right brains → Immunostaining
Left brains → Sarkosyl fractionation
0
2
(months)
b
Non-injected
WT tau
P301L/S320F tau
AT8
c
DAPI
AT8
100 μm
d
AT8 positive area coverage in MPtA (%)
ns
Non-injected
WT
P301L/S320F
e
f
AT8 positive area coverage in CA2 (%)

Fig. 2

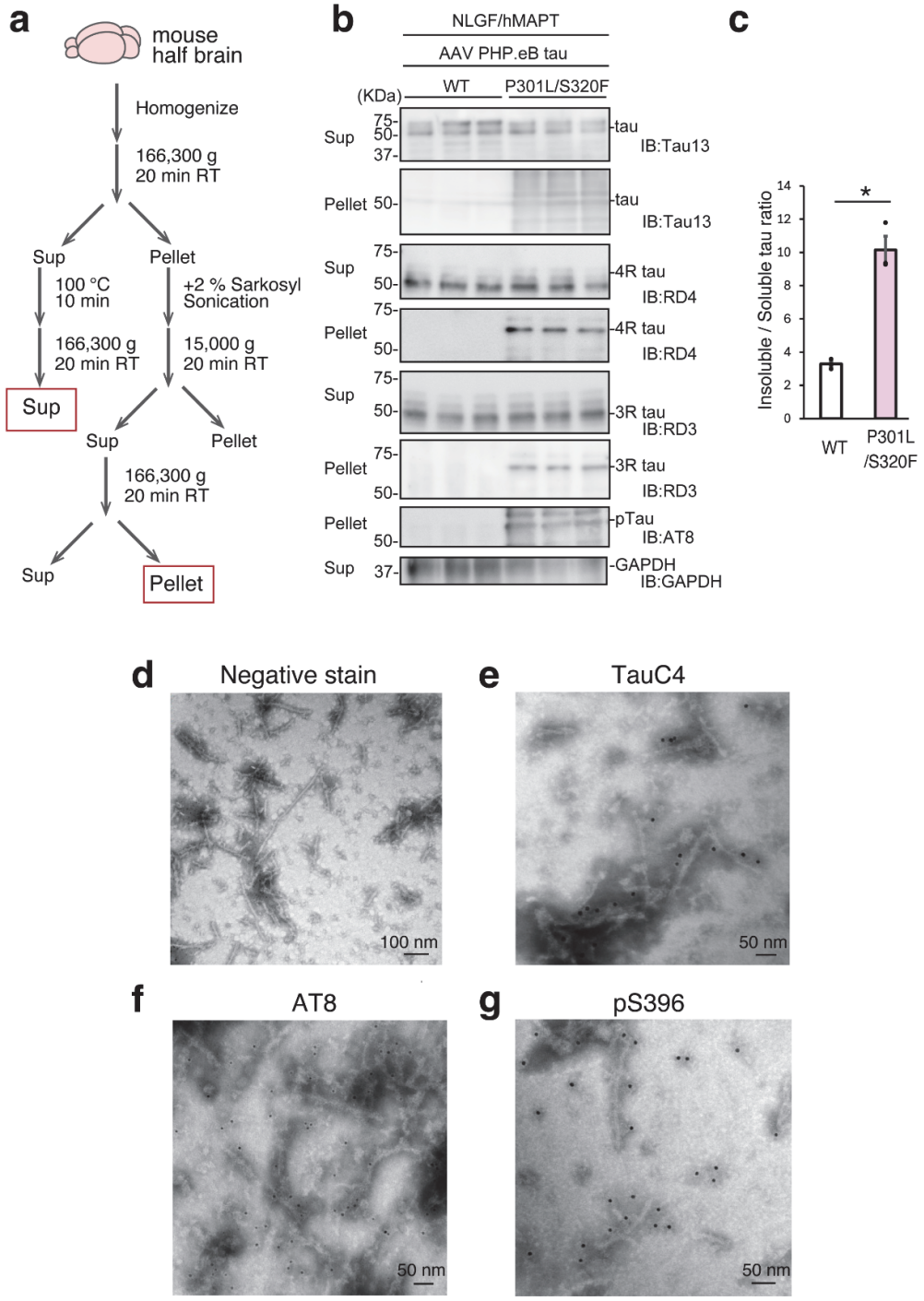
a
mouse
half brain
Homogenize
166,300 g
20 min RT
Sup
Pellet
100 °C
10 min
+2 % Sarkosyl
Sonication
166,300 g
20 min RT
15,000 g
20 min RT
Sup
Sup
Pellet
166,300 g
20 min RT
Sup
Pellet
b
NLGF/hMAPT
AAV PHP.eB tau
(KDa)
WT
P301L/S320F
Sup
Pellet
tau
IB:Tau13
4R tau
IB:RD4
3R tau
IB:RD3
pTau
IB:AT8
GAPDH
IB:GAPDH
c
Insoluble / Soluble tau ratio
WT
P301L
/S320F
d
Negative stain
100 nm
e
TauC4
50 nm
f
AT8
50 nm
g
pS396
50 nm

Fig. 3

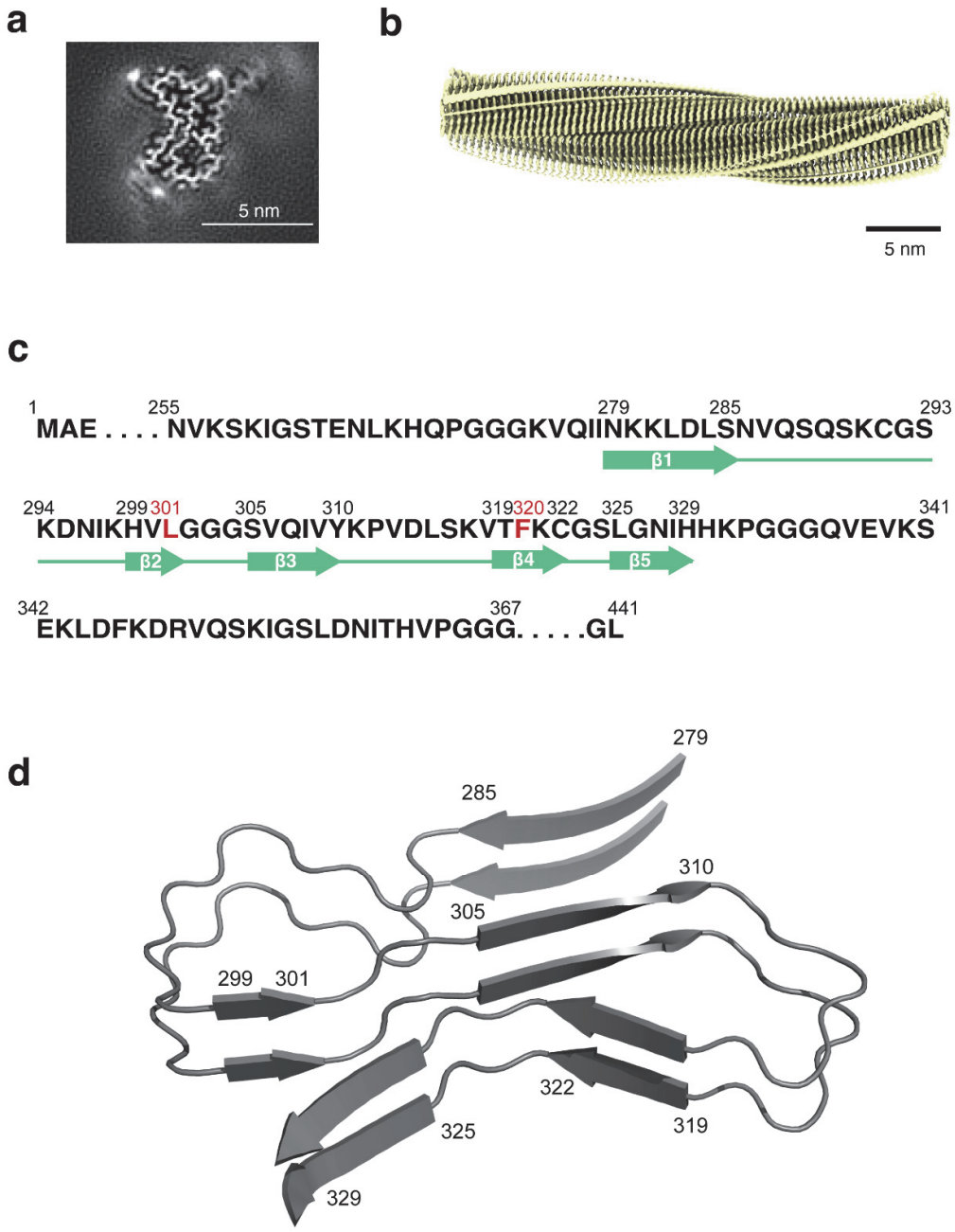
a
5 nm
b
5 nm
c
1 255 279 285 293
MAE . . . . NVKSKIGSTENLKHQPGGGKVQIINKKLDLSNVQSQSKCGS
β1
294 299 301 305 310 319 320 322 325 329 341
KDNIKHVLGGGSVQIVYKPVDLSKVTFKCGSLGNIHHKPGGGQVEVKS
β2 β3 β4 β5
342 367 441
EKLDFKDRVQSKIGSLDNITHVPGGG. . . . .GL
d
279
285
310
305
299 301
322
325
319
329

Fig. 4

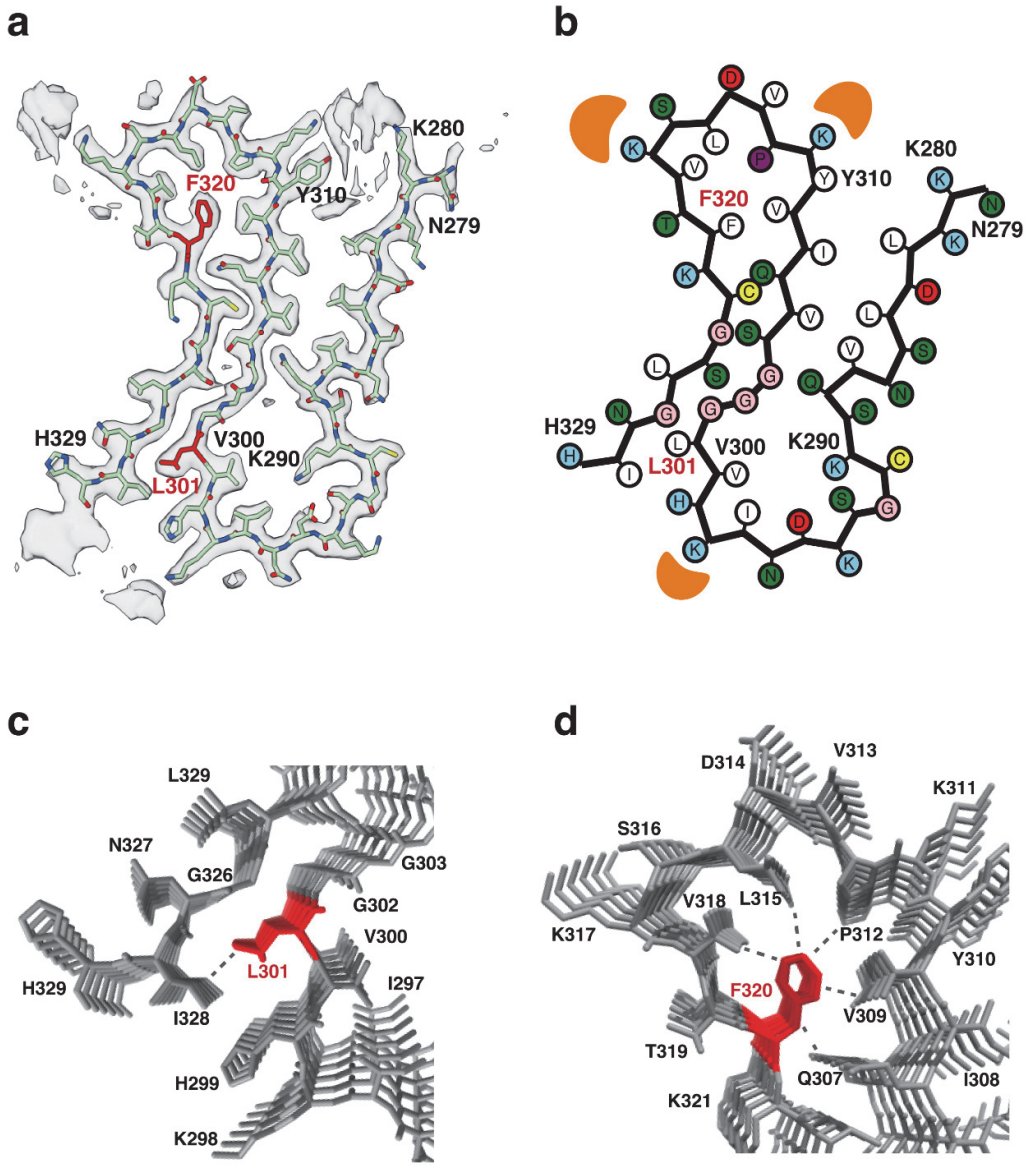

944

945 **Fig. 5**

946

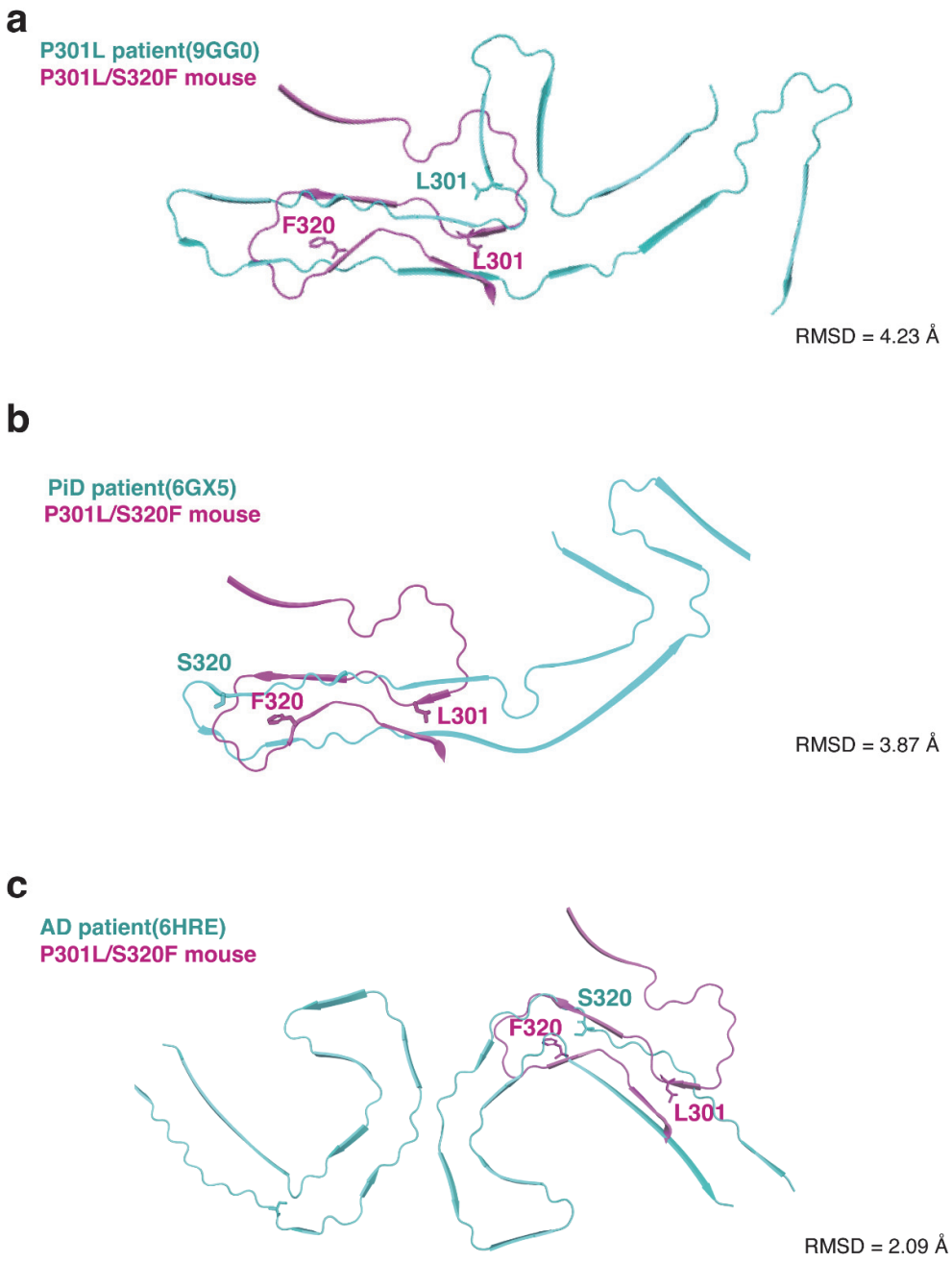
a
P301L patient(9GG0)
P301L/S320F mouse
L301
F320
L301
RMSD = 4.23 Å
b
PiD patient(6GX5)
P301L/S320F mouse
S320
F320
L301
RMSD = 3.87 Å
c
AD patient(6HRE)
P301L/S320F mouse
S320
F320
L301
RMSD = 2.09 Å

947

948 **Fig. 6**